Autonomic Neuroscience: Basic and Clinical 261 (2025) 103318

Contents lists available at ScienceDirect

Autonomic Neuroscience: Basic and Clinical

journal homepage: www.elsevier.com/locate/autneu

Symmetric projection attractor reconstruction: Transcutaneous auricular vagus nerve stimulation for visually induced motion sickness

Emmanuel Molefi [a,b,*], Ian McLoughlin [c], Ramaswamy Palaniappan [a]

[a] School of Computing, University of Kent, Canterbury, United Kingdom
[b] CNNP Lab[1], School of Computing, Newcastle University, Newcastle upon Tyne, United Kingdom
[c] ICT Cluster, Singapore Institute of Technology, Singapore, Singapore

ARTICLE INFO

Keywords:
Motion sickness
Transcutaneous auricular vagus nerve stimulation
Autonomic neuromodulation
Electrocardiography
Symmetric projection attractor reconstruction
Electrocardiogram morphology
Machine learning

ABSTRACT

Motion sickness is an enigma that has plagued humans for millennia – and could be exacerbated by automated vehicles and virtual reality. Here, we examined the neuromodulatory effects of transcutaneous auricular vagus nerve stimulation (taVNS) – a non-invasive brain stimulation tool – on autonomic function in response to motion sickness-induced nausea. We conducted a crossover randomized controlled study of healthy participants (n = 29) administered with active taVNS and sham, concurrent with visually-induced motion sickness during electrocardiogram (ECG) acquisition. Using symmetric projection attractor reconstruction (SPAR), a recent mathematical tool that computes images ("attractors") of morphology and variability of any approximately periodic signals, we show that taVNS induces a significant reduction in measures derived from these attractor image data, compared to sham. Notably, we found that a taVNS-evoked decrease in peak theta density showed a marked correlation with improvements in motion-induced nausea symptom severity. Furthermore, the use of machine learning revealed differential discriminatory power of taVNS response with an area under the receiver operating characteristic curve (AUC) of 0.81. Taken together, these findings provide novel insights into taVNS for motion-induced nausea; and additionally suggest that ECG SPAR-based features may be important for evaluating taVNS therapy response — with implications for adaptive taVNS.

1. Introduction

In most people – except those with bilateral loss of labyrinthine function – sensory conflict triggers motion sickness, a complex physiological response to real, perceived, or virtual motion. Despite its ubiquity, motion sickness remains a persistent, debilitating, and elusive malady. Moreover, some individuals are notoriously prone to this syndrome; for instance, individuals who experience migraine headaches (Marcus et al., 2005), and those with history of traumatic brain injury (Classen and Owens, 2010).

Although motion sickness is primarily characterized by nausea and vomiting, its polysymptomatic onset includes a conglomeration of features such as cold sweating, dizziness, and drowsiness, among others — which detrimentally influence task performance and cognitive function (Gresty et al., 2008; Gresty and Golding, 2009; Matsangas et al., 2014). Thus, given these negative effects, the minimal advancements in novel therapeutic methods toward motion sickness management, and the undesirable side effects that accompany mainstay pharmaceutical agents (Lackner, 2014); new, innovative therapeutic tools are needed to mitigate motion sickness. One such avenue may be transcutaneous auricular vagus nerve stimulation (taVNS).

We have long known that cervical vagus nerve stimulation (VNS) has therapeutic benefits; particularly, for ailments such as refractory epilepsy and depression (Ben-Menachem et al., 1994; Handforth et al., 1998). We now know that this neurostimulation tool has broad clinical potential. However, VNS carries risks due to its invasive nature, including potential post-operative complications (Ben-Menachem et al., 2015; Hilz, 2022). Modern research has revealed that non-invasive VNS derivatives such as taVNS hold promise as modalities of VNS (Badran et al., 2018a). Additionally, evidence is mounting that tragus stimulation, in particular, elicits differential autonomic effects (Badran et al., 2017, 2018b); in part because the vagus nerve (10th cranial nerve) is considered a major neural substrate of the parasympathetic nervous system – a component of the autonomic nervous system (ANS), alongside the sympathetic nervous system, and the less well-known enteric nervous system – thus portraying a pivotal role in ANS function regulation (Murray et al., 2016; Butt et al., 2020).

* Corresponding author.
E-mail addresses: emmanuel.molefi@ncl.ac.uk (E. Molefi), ian.mcloughlin@singaporetech.edu.sg (I. McLoughlin), r.palani@kent.ac.uk (R. Palaniappan).
[1] www.cnnp-lab.com.

https://doi.org/10.1016/j.autneu.2025.103318
Received 12 November 2024; Received in revised form 10 May 2025; Accepted 21 June 2025
Available online 11 July 2025

taVNS mechanism of action is thought to be mediated by the projection of afferent signaling toward the nucleus tractus solitarii (NTS) of the medulla and, in turn, activating the locus-coeruleus-norepinephrine system. Afferent signals are also projected beyond the NTS to other important brain structures, including locus coeruleus and the dorsal raphe nuclei (Ellrich, 2019; Butt et al., 2020; Hilz, 2022). Whereas VNS and transcutaneous cervical VNS (tcVNS) target the cervical branch of the vagus nerve (which courses from the brainstem to the colon), taVNS engages the auricular branch. Herein, we consider taVNS because of advantages which include (among others) easy and accurate application compared to tcVNS (Kim et al., 2022).

Previous research on ANS activity in taVNS and motion sickness has commonly performed analysis of electrocardiogram (ECG)-derived heart rate variability (HRV) (Carandina et al., 2021; Irmak et al., 2021; Molefi et al., 2023a). Here, to glean insights from the ECG data directly, we leverage the recently developed symmetric projection attractor reconstruction (SPAR) method. SPAR is a mathematical tool that facilitates visualization and quantification of morphology (shape) and variability of any approximately periodic waveform by computing two-dimensional (2D) images ("attractors") (Aston et al., 2018; Nandi and Aston, 2020; Lyle and Aston, 2021). Previously, SPAR has been applied to various biomedical signals, including the ECG (Lyle et al., 2019), microvascular blood flux (Thanaj et al., 2019), and photoplethysmogram (PPG) (Hörandtner et al., 2022).

In this study, our main aim is to examine ECG morphology and variability response to taVNS versus sham in tandem with nauseogenic visual stimulation via SPAR-based measures. We also evaluate whether potential differential effects of taVNS on these measures may be linked to the subjective effects of taVNS in motion-induced nausea. Furthermore, we perform machine learning analysis to determine taVNS response from information captured by these SPAR metrics.

2. Methods

2.1. Participants

In this study, we analyzed physiological and behavioral data from 29 healthy participants (mean ± SD = 23.7 ± 6.8 years, age range = 18–49 years, 21 females) who provided written informed consent, had normal or corrected-to-normal vision, and were not on any medication. The previously validated motion sickness susceptibility questionnaire short-form (MSSQ-Short) (Golding, 2006) was used as a pre-participation screening tool; whereby participants with a percentile score > 60 (corresponding to an MSSQ-Short raw score of 14.36) were recruited, based on prior research (e.g., Sclocco et al., 2016; Toschi et al., 2017). The MSSQ-Short asks participants to recall experiences of nausea or vomiting at childhood (below 12 years of age; MSA), and over the last decade (MSB) following various transport or entertainment modalities. Participants received a £30 Amazon gift voucher for their participation. All procedures were approved by the University of Kent Central Research Ethics Advisory Group (ref: CREAG015-12-2021), and conformed to the Declaration of Helsinki standards for human research.

2.2. Experimental protocol

We used a randomized, sham-controlled, crossover experimental design (Fig. 1c, d). Participants underwent two sessions of electrical stimulation via two lab visits that were scheduled at least 1 week apart for washout of any stimulation effects; the sessions were carried out in randomized order. For each lab visit, participants were exposed to a contiguous visual stimulus, wherein at baseline, observed a black crosshair for 10 min, followed by a nauseogenic visual stimulus (see Section 2.3) concurrent with electrical stimulation (see Section 2.4) for a maximum of 20 min, and finally, a recovery period presented similar to baseline (Fig. 1d). During nauseogenic visual stimulation, participants recorded their subjective level of nausea – not cued – via a keypad press (0 = "no nausea"; 1 = "mild"; 2 = "moderate"; and 3 = "strong"). Participants were instructed to provide a rating when they felt a change in the intensity of nausea they were experiencing. The keypad also allowed participants to stop presentation of the nauseogenic visual stimulus when on the verge of vomiting — triggering automatic launch of the recovery period. Electrical stimulation was delivered at the left tragus during active taVNS lab visits (Fig. 1a), and at the left earlobe during sham lab visits (Fig. 1b). For safety reasons and smooth running of the experiment, the experimenter was present in the lab but kept out of view. ECG acquisition was performed continuously between baseline onset and recovery offset, during which participants were required to minimize body movements and conversation, and to focus on stimuli presentation. To measure the severity of motion sickness, participants completed a pre- and post-treatment motion sickness assessment questionnaire (MSAQ) (Gianaros et al., 2001) and simulator sickness questionnaire (SSQ) (Kennedy et al., 1993). The MSAQ instrument contains 16 symptoms with a Likert-type scale (1–9 = "not at all" to "severely") that quantify the gastrointestinal, central, peripheral and sopite-related dimensions of motion sickness. Calculation of the MSAQ total and subscale scores was guided by Gianaros et al. (2001). Included in the SSQ are 16 symptoms with a Likert-type scale (0–3 = "none" to "severe") that are clustered into nausea, oculomotor and disorientation factors of motion sickness. SSQ total and subscale factors were scored following guidance in Kennedy et al. (1993). It is worth noting that there are important differences between the MSAQ and SSQ with the latter being explicitly derived from the former to address shortcomings that arise when assessing sickness in simulation scenarios as opposed to real-life situations (e.g., during a car ride or on a ship). Herein, while we include both, the SSQ is expected to provide a more relevant result.

2.3. Nauseogenic stimulus

For nausea induction, we developed a nauseogenic visual stimulus as alternating black and white vertical stripes with left-to-right circular motion at 62.5°/s in MATLAB (The MathWorks, Inc., Natick, MA, USA) using the Psychophysics Toolbox Version 3 (Psychtoolbox-3.0.19; http://www.psychtoolbox.org) (Brainard, 1997; Pelli, 1997; Kleiner et al., 2007). Visual stimulation was presented with a 47-inch LG LCD widescreen (47LW450U, LG Electronics UK, UK) at a refresh rate of 60 Hz, for a maximum of 20 min or until interruption. For an unimpeded field-of-view, participants viewed the stimulus at a distance filling their visual field. Viewing of the horizontal translation of the visual stripes is known to instigate illusory self-motion. Further, the nauseogenic visual stimulation administered here provokes motion-induced nausea via visual input akin to that of a rotating optokinetic drum (Bos and Bles, 2004; Levine et al., 2014). Of note, this visual stimulus is similar to that described previously (Molefi et al., 2023b). An fMRI-compatible variant of the stimulus has been used for nausea induction in prior work (e.g., Toschi et al., 2017).

2.4. Electrical stimulation

We administered taVNS via the EM6300 A TENS device (Med-Fit UK Ltd, Stockport, UK); applying current-controlled asymmetric biphasic square-wave electric pulses of 200 μs at 20 Hz continuously for at most 20 min. Previous studies of comparable protocols were reviewed to select these stimulation parameters (e.g., Beh and Friedman, 2019; Tran et al., 2019; Cao et al., 2021). The electrical current was delivered at the tragus of the left ear for taVNS (mean ± SD = 6.03 ± 2.40 mA) (Fig. 1a), and to the left earlobe for sham (5.55 ± 3.41 mA) (Fig. 1b). This electric current was comparable in both conditions (p = 0.4440, Wilcoxon signed rank test). Importantly, this suggests that our stimulation protocol, wherein we delivered taVNS at the tragus and sham at the earlobe – a site not innervated by the auricular branch of the vagus nerve (Peuker and Filler, 2002; Bermejo et al., 2017; Yakunina et al., 2017) – provided a good control condition for taVNS administration.

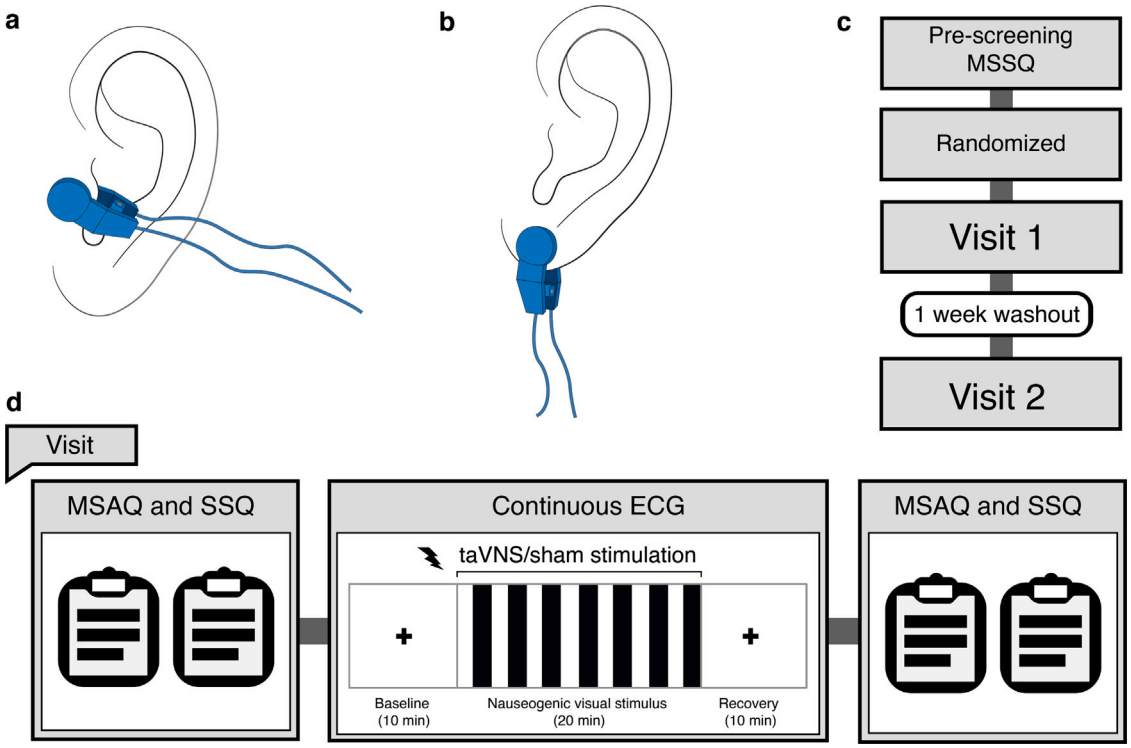

Fig. 1. Experimental overview illustrations. (**a**) For active taVNS, the electrode was clipped to the tragus of the left ear. (**b**) And clipped to the left earlobe for sham stimulation. (**c**) The schematic of the randomized, sham-controlled, crossover design timeline. (**d**) For a typical lab visit, participants completed a pre and post motion sickness assessment questionnaire (MSAQ) and simulator sickness questionnaire (SSQ); additionally, participants underwent a baseline period, followed by nauseogenic visual stimulation concurrent with electrical stimulation (taVNS or sham), then a recovery period, while electrocardiogram (ECG) acquisition was performed.

All participants were taVNS-näive. Prior to the experiments, intensity of stimulation current was tested and tailored for each participant via a one-up/one-down staircase procedure. All participants reported perception of the stimulation current without painful sensation. taVNS effects were well-tolerated by all participants, and no one reported adverse events. During stimulation, a countdown timer on the electrical stimulator was set to elapse simultaneous with presentation of the nauseogenic visual stimulus; and because participants could interrupt the visual stimulus due to developing severe nausea, switching off the electrical stimulator was performed by the experimenter accordingly.

2.5. ECG data acquisition and preprocessing

ECG data were continuously recorded using the BioSemi ActiveTwo system (BioSemi B. V., Amsterdam, Netherlands), with a sampling frequency of 256 Hz (Fig. 1d). To perform ECG signal preprocessing, we used custom scripts developed in MATLAB (R2023b and R2024a). Following visual inspection to identify disturbances and distortions, the ECG signals were filtered between 0.5 and 30 Hz (Dennison et al., 2016) to eliminate baseline wander and muscle noise using a 4th-order Butterworth bandpass IIR filter. To remove electrical stimulation-evoked artifact, a Butterworth notch IIR filter was applied at 20 Hz. We performed zero-phase filtering to avoid phase distortion. Finally, the artifact-free ECG time series were then used to extract 5 min epochs at "baseline", "stimulation", and "recovery". The "baseline" epoch was obtained from the end of the Baseline period shown in Fig. 1d; that is, prior to nauseogenic stimulus onset. Likewise, the "stimulation" epoch was obtained from the end of the Nauseogenic visual stimulus period shown in Fig. 1d. That of "recovery" was obtained from the beginning of the Recovery period depicted in Fig. 1d. These epochs were composed of several segments (each of 10 s) combining to a total of 5 mins. Importantly, the timeframe for extracting these 5 min epochs was consistent across all participants.

2.6. SPAR analysis

To quantify ECG morphology and variability, we applied SPAR — a novel mathematical tool inspired by nonlinear dynamical systems, that transforms any approximately periodic signal into a two-dimensional representation ("attractor") (Aston et al., 2018; Nandi et al., 2018; Nandi and Aston, 2020; Lyle and Aston, 2021). Prior to performing SPAR, we obtained the de-noised ECG data from above (see Section 2.5), partitioned it into 10 s epochs, and range normalized it to the interval $[0, 1]$. As a brief overview of the SPAR method – based on its original implementation (Aston et al., 2018) – for an ECG time series $x(t)$ (Fig. 2a), the time delay is determined by computing $\tau = T/3$, where T is the average cardiac cycle length, that is, the mean of the RR intervals; R-peak detection was performed using the Pan-Tompkins algorithm (Pan and Tompkins, 1985). Next, $N = 3$ points are placed at equal distances of τ by performing Takens' delay coordinate embedding (Takens, 1981) via

$$y(t) = x(t - \tau), \qquad z(t) = x(t - 2\tau). \tag{1}$$

The embedded points can then be plotted in three-dimensional (3D) phase space where their trajectories can be observed (Fig. 2b); if followed, the $N = 3$ points we started with demonstrate evolvement in phase space — generating numerous overlapping loops in the process. For the next step, to remove baseline shift (for example, which may result from respiration and movement), the 3D reconstructed attractor is projected onto a plane (v, w) that is orthogonal to the vector $[1, 1, 1]$ using

$$v = \frac{1}{\sqrt{6}}(x + y - 2z), \qquad w = \frac{1}{\sqrt{2}}(x - y). \tag{2}$$

Despite Fig. 2c showing the degree of overlap between trajectories of the embedded points, this information is masked, and only becomes revealed when a density (i.e., heatmap) is overlaid; this addition of

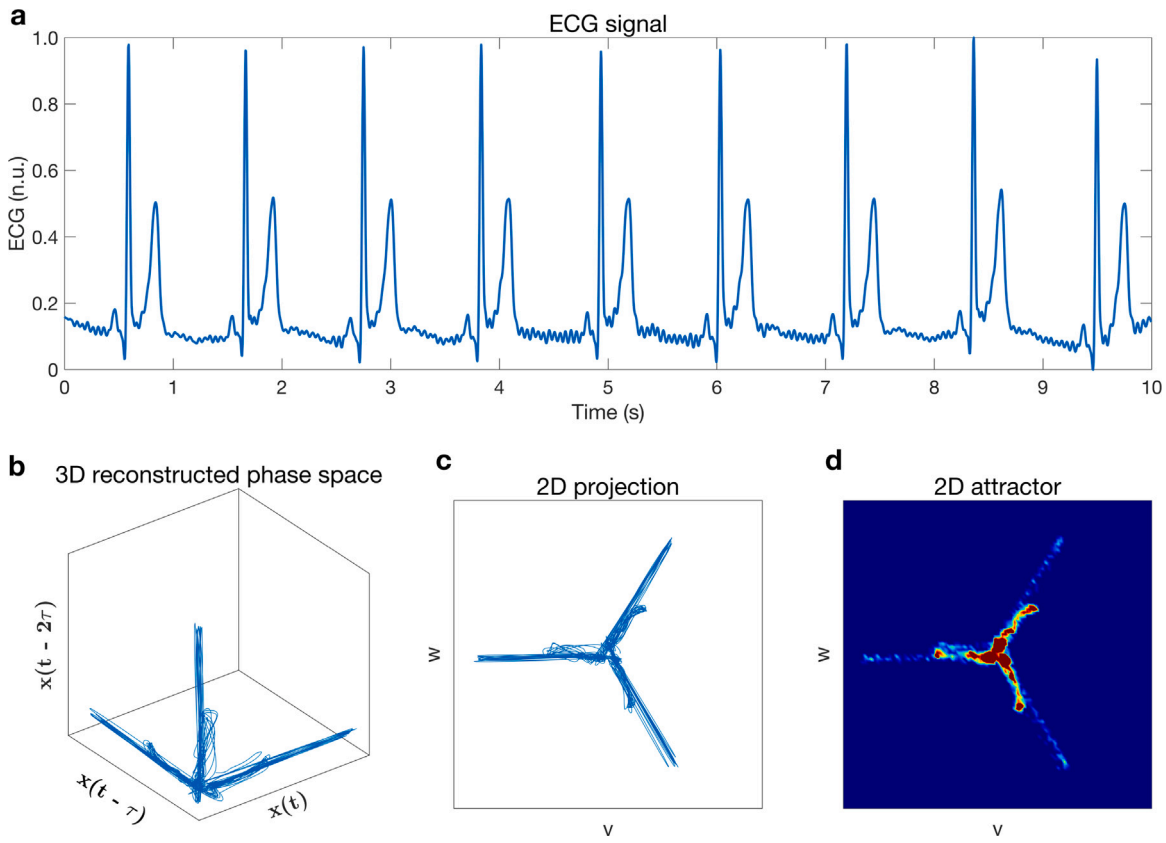

Fig. 2. Generation of a two-dimensional (2D) attractor from an electrocardiogram (ECG) signal. (**a**) A 10 s ECG signal for one example participant. (**b**) A three-dimensional (3D) reconstructed attractor for $N = 3$ embedding using Takens' delay coordinates. (**c**) A 3D reconstructed attractor projected onto a plane (v, w) perpendicular to the vector $[1, 1, 1]$. (**d**) A 2D attractor overlaid with a density (i.e., heatmap).

color provides information about most frequented regions (Fig. 2d; Supplementary Video S1).

Owing to the complexity of the ECG waveform, herein we use the extended SPAR method (Lyle and Aston, 2021), wherein an ECG time series $x(t)$ with period T is embedded into $N \geq 3$ dimensions using the time delay $\tau = T/N$ by the coordinates $x_{N,j}(t) = x(t - j\tau)$, $j = 0, \ldots, N - 1$; Lyle and Aston (2021) then define $a_{N,k}(t)$ and $b_{N,k}(t)$ coordinates as

$$a_{N,k}(t) = \frac{1}{\sqrt{N}} \sum_{j=0}^{N-1} \cos(2\pi jk/N) x_{N,j}(t),$$
$$b_{N,k}(t) = -\frac{1}{\sqrt{N}} \sum_{j=0}^{N-1} \sin(2\pi jk/N) x_{N,j}(t) \quad (3)$$

for $k = 1, \ldots, \lfloor (N-1)/2 \rfloor$. In this study, we use $k = 1$ for all embedding projections. Fig. 3 shows example attractors obtained via this implementation. Following attractor generation, in addition to maximal density, we extracted the peak values of the radial density distribution, theta density distribution, and attractor outline in the θ direction, as attractor measures, according to previously described methods (Lyle et al., 2021). A detailed description of how these attractor measures were quantified, including their physiological interpretation is provided in Table 1; furthermore, Fig. 4 provides an illustration of how the measures were computed from the attractors.

Importantly, the rationale for computing these features (Table 1) with regards to motion-induced nausea stems from previous evidence showing that increases in malaise severity trigger high levels of autonomic arousal via a reduction in parasympathetic neural activity (Kim et al., 2011; LaCount et al., 2011; Molefi et al., 2023a). Given that elevated autonomic arousal has been associated with significantly increased T wave amplitude (Gray et al., 2007), we surmise that changes in peak radial density – which captures the morphology of the T wave (Table 1) – may reveal differences in participants under taVNS versus sham. Similarly, beat-to-beat variability measures such as peak theta density and maximal density may help differentiate motion-induced nausea based on the notion that lower beat-to-beat variability would indicate heightened malaise. A reduction in the R peak amplitude would indicate stress (Doi et al., 1983); therefore, peak attractor outline – which corresponds to R peak amplitude (Table 1) – may reveal the development of motion-induced nausea as participants exhibit agitation.

2.7. Machine learning

To perform classification of electrical stimulation type, active versus sham taVNS, we trained discriminant analysis, ensemble (with AdaBoostM1 and LogitBoost), logistic regression, naïve Bayes, neural network, and support vector machine (with Gaussian, linear, polynomial, and sigmoid kernels), classifiers as implemented by the functions fitcdiscr, fitcensemble, fitckernel, fitcnb, fitcnet, and fitcsvm, respectively, in MATLAB 2023b. The output of the classifiers was two classes corresponding to taVNS versus sham. We provided as input attractor features constructed by deriving attractor measures obtained from the "stimulation" interval as percentage change from "baseline" attractor measures (for each participant at each condition).

For model training, we used the leave-one-participant-out cross-validation (LOPOCV) procedure; that is, all data for one participant were excluded from the training dataset and used for generalization. Of note, LOPOCV is well-known as leave-one-subject-out cross-validation (LOSO-CV), a term utilized by Gurel et al. (2020) for examination of target engagement detection in tcVNS for traumatic stress triggers; importantly, this procedure ensures that the training dataset would not

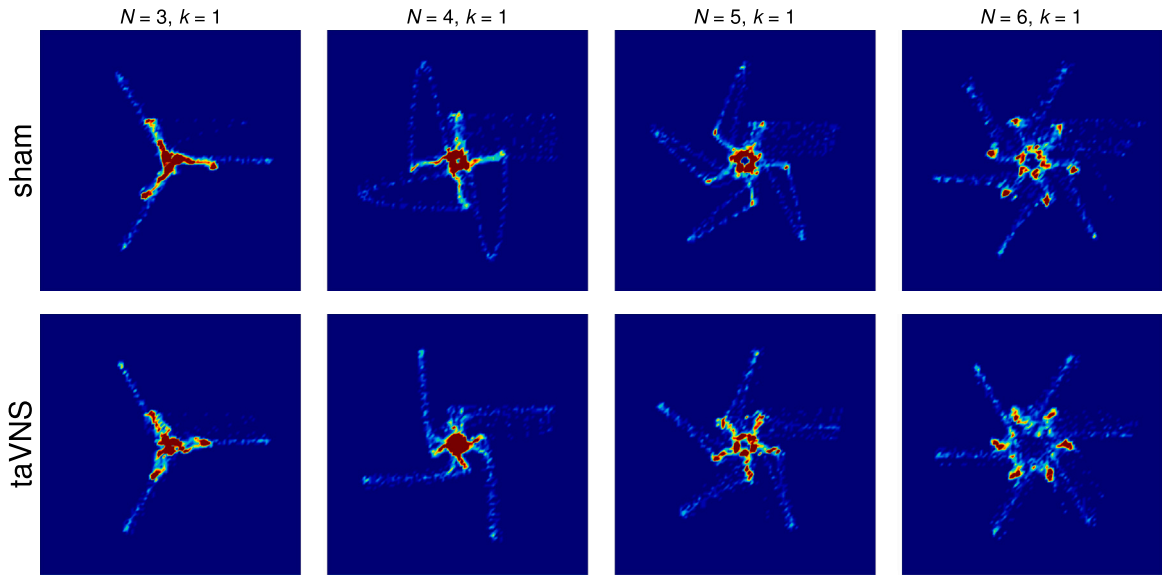

Fig. 3. Electrocardiogram (ECG)-derived symmetric projection attractor reconstruction (SPAR) images in response to sham and taVNS. (**sham**) The (N, k) attractors generated from a 10 s ECG signal of one example participant for $N = 3, 4, 5, 6$ embeddings from sham condition, (**taVNS**) and taVNS condition.

Table 1
Summary of attractor measures including their physiological interpretation.

Attractor parameter	Description	Physiological interpretation
Peak radial density	The distance from the center to the outer edge of the attractor is divided into 50 bins; then starting at the attractor center, the sum of the density values in each bin is computed to construct a distribution — from which a peak value is obtained (Fig. 4a).	This measure reflects changes in the morphology of the T wave; with lower values indicating a reduced T wave amplitude.
Peak theta density	Angles are uniformly spaced on the attractor into 100 bins starting at 0 degrees; to obtain a θ density distribution, a summation of the density values in each bin is performed; a peak value is then extracted from the constructed distribution. Please note that this measure captures the most dense parts of the attractor at a particular θ from the attractor center (Fig. 4b).	Higher values of this measure indicate lower beat-to-beat variability.
Peak attractor outline	This combines the aforementioned radial and angular methods to compute the outline (perimeter) of the attractor as the maximum r in the θ direction; then a peak value is obtained from the resultant profile (Fig. 4c).	Higher values of this measure correspond to a larger attractor, which indicates an increase in waveform amplitude, and thus quantifies changes in waveform morphology; for example, higher R peak amplitude results in longer attractor arms — and in turn, a larger attractor.
Maximal density	This computes the histogram of the attractor, then obtains the maximum value. Please note that this measure captures the most frequented region in the entire attractor (Fig. 4d).	Higher values of this measure indicate lower beat-to-beat variability.

contain data of the test participant. This procedure was iterated for each of the 29 participants. To find hyperparameters that minimize five-fold, ten-fold, and leave-one-participant-out cross-validation loss, we used Bayesian optimization with 100 iterations. Please note that the LOPOCV procedure used for model training herein was nested with five-fold, ten-fold, and LOPOCV cross-validation options for hyperparameter optimization; and that left unspecified, the above-mentioned MATLAB functions – fitcsvm, for example – would find hyperparameters that minimize five-fold cross-validation loss. In essence, our model setup was a nested cross-validation where the inner loops for hyperparameter optimization were run with three different settings (five-fold, ten-fold, and leave-one-participant-out cross-validation), and the outer loops were always run with leave-one-participant-out cross-validation. In this context, it is important to note that our small sample size of $n = 29$ would lead to a very small group size within each fold for the ten-fold cross-validation.

For model evaluation, we computed the area under the receiver operating characteristic curve (AUC), which is a robust metric of classification performance; whereby an AUC of 1 represents perfect classification and an AUC of 0.5 corresponds to random classification. The statistical property of the AUC is equivalent to the nonparametric Wilcoxon rank sum test; that is, representing the probability with which the model ranks a randomly chosen positive instance higher than a randomly chosen negative instance. All experiments were performed on a node consisting of a single 80 GB NVIDIA A100 GPU.

2.8. Statistical analysis

All statistical analyzes were performed using MATLAB. A two-way repeated-measures ANOVA with within-subjects factors "time" (pre vs. post) and "stimulation" (taVNS vs. sham) followed by post-hoc paired t-tests was used for range normalized MSAQ and SSQ scores. Attractor measures were averaged across all four embeddings (i.e., $N = 3, 4, 5, 6$), and then computed as $\Delta = 100((X - X_0)/X_0)$, where X denotes "stimulation" or "recovery" intervals, and X_0 denotes "baseline". Percentage changes in attractor measures were analyzed with two-way repeated measures ANOVAs with within-subjects factors "time" (pre vs. during vs. post) and "stimulation" (taVNS vs. sham) followed by post-hoc paired t-tests using Bonferroni to correct for multiple comparisons when significant interactions were seen. Effect sizes were computed using the unbiased estimate of robust Cohen's d. Descriptors for robust Cohen's d are interpreted as ($d < 0.2 \rightarrow$

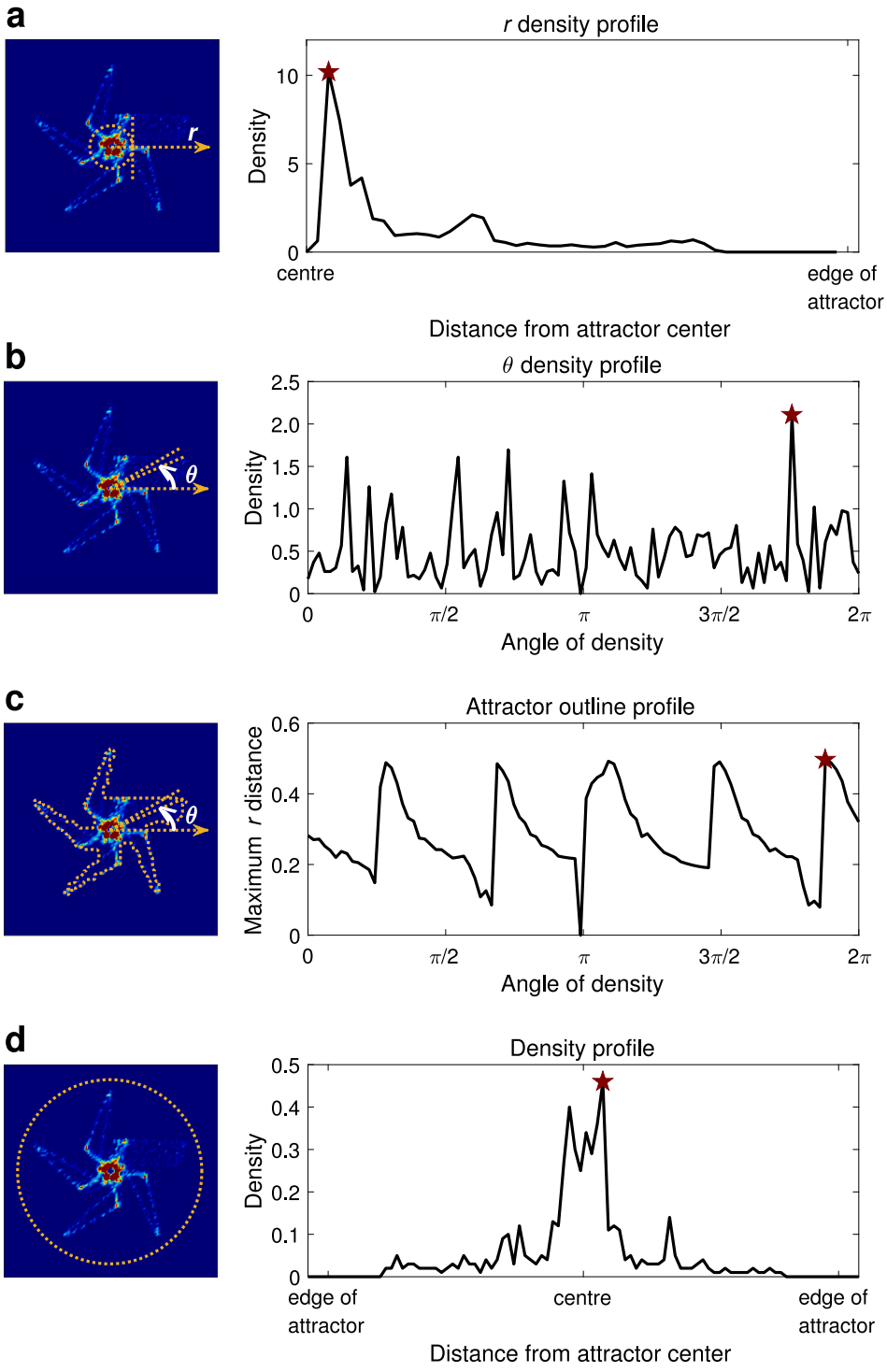

Fig. 4. Illustration of how the attractor measures were computed. (**a**) The radial density distribution is constructed from the sum of density values in each of the 50 bins along the distance from the attractor center to the outer edge; then a peak value obtained. (**b**) To obtain a θ distribution, the sum of density values in each of the 100 bins of uniformly spaced angles on the attractor is computed; then a peak value obtained. (**c**) Here the radial and angular methods are combined to compute the attractor outline as the maximum r in the θ direction with the peak extracted from the resultant profile. (**d**) The histogram of the attractor is computed and a maximum value obtained. See Table 1 for the physiological interpretation of these measures.

'negligible'; $d < 0.5$ → 'small'; $d < 0.8$ → 'medium'; $d \geq 0.8$ → 'large') (Cohen, 2013). To probe for possible relationships between percent changes in attractor measures (expressed as difference of differences, i.e., $\text{taVNS}_{\text{during–pre}} - \text{sham}_{\text{during–pre}}$ or $\text{taVNS}_{\text{post–pre}} - \text{sham}_{\text{post–pre}}$) and range normalized behavioral measure changes (likewise computed as difference of differences, i.e., $\text{taVNS}_{\text{post–pre}} - \text{sham}_{\text{post–pre}}$), or MSB scores (expressed as absolute values), we computed Spearman's rank correlation coefficient (expressed as Spearman ρ), and used the Bonferroni method to correct for multiple comparisons. Data are expressed as median and quartiles, or mean ± standard error of the mean (SEM). All statistical tests were two-tailed at ($p < 0.05$). To evaluate machine-learning models, we computed the

area under the receiver operating characteristic (ROC) curve (AUC) metric.

3. Results

The mean ± SD (range) MSSQ-Short scores of the included participants ($n = 29$) was 27.84±8.52 (15.75−48.00), with MSSQ-Short subscale scores of (MSA = 13.61±5.53 [mean ± SD]; MSB = 14.23±4.95). To establish that the nauseogenic visual stimulation induced motion sickness, we examined the participant's subjective level of nausea ratings in the sham condition; this analysis revealed a correlation between median nausea rating and time to peak nausea (Spearman $\rho = -0.51$, $p = 0.0047$). Participants exhibited no notable changes in the scores of the MSAQ total and subscale responses between taVNS and sham. For the SSQ instrument, the SSQ total, oculomotor, and disorientation measures did not indicate any marked interactions (stimulation × time) between taVNS and sham; however, we observed improvements in SSQ nausea factor scores (two-way repeated measures ANOVA; stimulation, $F_{1,28} = 10.76$, $p = 0.0028$; time, $F_{1,28} = 23.04$, $p = 4.79 \times 10^{-5}$; stimulation × time interaction, $F_{1,28} = 4.29, p = 0.0476$; with Bonferroni's post-hoc correction) with taVNS versus sham. To further examine the efficacy of the nauseogenic visual stimulation in inducing motion sickness, we compared the SSQ nausea factor scores before and after the induction in the sham condition; and found a significant increase in nausea ($t = -4.36$, $p = 0.0002$, $d = -1.17$). Notably, no participants in our study vomited during or after nausea induction.

While a two-way repeated measures ANOVA revealed a significant effect of time only ($F_{2,56} = 5.12$, $p = 0.0090$) for peak radial density responses (averaged across all embeddings) between taVNS and sham, we observed a significant effect of stimulation ($F_{1,28} = 10.25$, $p = 0.0034$), time ($F_{2,56} = 12.48$, $p = 3.30\times10^{-5}$), and an interaction ($F_{2,56} = 6.02$, $p = 0.0043$) for peak theta density; and post-hoc analysis (with Bonferroni correction) revealed a taVNS-induced reduction in peak theta density responses during stimulation ($t = 2.76$, $p = 0.0101$, $d = -0.83$; Fig. 5b), as well as post-stimulation ($t = 2.91$, $p = 0.0069$, $d = -0.95$; Fig. 5f). Moreover, we found significant differences between taVNS and sham in maximal density responses (two-way repeated measures ANOVA; stimulation, $F_{1,28} = 7.92$, $p = 0.0088$; time, $F_{2,56} = 8.42$, $p = 0.0006$; stimulation × time interaction, $F_{2,56} = 4.02$, $p = 0.0234$). Post-hoc analysis showed a marked reduction in maximal density during stimulation ($t = 2.42$, $p = 0.0223$, $d = -0.77$; Fig. 5d), and following stimulation ($t = 2.47$, $p = 0.0199$, $d = -0.66$; Fig. 5h) with taVNS versus sham. For peak attractor outline responses, we did not observe a significant stimulation × time interaction.

For additional analyses, we computed correlations between MSB scores (expressed as absolute values) and range normalized changes in SSQ nausea scores (computed as difference of differences, i.e., $taVNS_{post-pre} - sham_{post-pre}$), and percent changes in attractor measures that revealed marked significance, which were likewise calculated as difference of differences (specifically, $taVNS_{during-pre} - sham_{during-pre}$ for the taVNS vs. sham contrast; and $taVNS_{post-pre} - sham_{post-pre}$ for the post-taVNS vs. post-sham contrast) (Table 2). MSB scores are used here because these are adult-based motion sickness susceptibility scores. As shown in Table 2, maximal density during taVNS versus sham demonstrated a high positive correlation with MSB (Spearman $\rho = 0.52$, $p = 0.0040$); however, this significance was not observed for the post-stimulation interval. We also found a marked negative correlation between peak theta density for post-taVNS versus post-sham with SSQ nausea scores.

We used machine learning to perform classification of stimulation type, active or sham taVNS, from 20 features extracted from attractors obtained at taVNS and sham sessions; Fig. 3 presents sample attractors for one example participant. Of the trained classifiers, an ensemble of boosted classification trees using adaptive logistic regression (LogitBoost) classifier demonstrated great performance when minimizing five-fold (AUC = 0.72) and ten-fold (AUC = 0.81) cross-validation loss (Table 3). Importantly, the results suggest that the classification ensemble (AdaBoostM1 and LogitBoost) models show above chance levels to reveal which electrical stimulation – taVNS or sham – a given participant received; in particular, when using five-fold and ten-fold cross-validation (Table 3). Notably, we observed that the AdaBoostM1 classifier also achieved an acceptable AUC score with nested LOPOCV (AUC = 0.72). Furthermore, as presented in Table 3, discriminant analysis, and SVM with linear kernel classifiers also obtained AUC values considered acceptable (AUCs > 0.7).

Table 2
Spearman's rank correlation coefficients between behavioral measures MSB scores and range normalized changes in SSQ nausea scores, and attractor measures derived during and following taVNS and sham stimulation. Specifically, MSB scores were calculated as absolute values; range normalized SSQ nausea scores were computed as difference of differences (i.e., $taVNS_{post-pre} - sham_{post-pre}$). Likewise, the presented percent changes in attractor measures were computed as difference of differences: $taVNS_{during-pre} - sham_{during-pre}$ for the taVNS vs. sham contrast; and $taVNS_{post-pre} - sham_{post-pre}$ for the post-taVNS vs. post-sham contrast. ΔΔ indicates difference of differences. MSB, over the last 10 years motion sickness susceptibility questionnaire (MSSQ) scores; SSQ, simulator sickness questionnaire; taVNS, transcutaneous auricular vagus nerve stimulation.

	MSB		ΔΔSSQ nausea	
	ρ	p-value	ρ	p-value
taVNS vs. sham				
ΔΔPeak theta density	0.25	0.1822	−0.35	0.0640
ΔΔMaximal density	**0.52**	**0.0040**	0.04	0.8342
Post-taVNS vs. Post-sham				
ΔΔPeak theta density	0.03	0.8600	**−0.44**	**0.0171**
ΔΔMaximal density	0.24	0.2088	−0.35	0.0594

Table 3
The AUC values of ten models for binary classification of taVNS therapy response derived using LOPOCV with nested 5-fold, 10-fold, and leave-one-participant-out cross-validation. Specifically, our model setup was a nested cross-validation where the inner loops for hyperparameter optimization were run with three different settings (five-fold, ten-fold, and leave-one-participant-out cross-validation), and the outer loops were always run with leave-one-participant-out cross-validation. It is important to note that our small sample size of $n = 29$ would lead to a very small fold size for the ten-fold cross-validation. AUC, area under the receiver operating characteristic (ROC) curve; taVNS, transcutaneous auricular vagus nerve stimulation; LOPOCV, leave-one-participant-out cross-validation; SVM, support vector machine.

Model	5-fold	10-fold	LOPOCV
Discriminant Analysis	**0.72**	0.69	**0.72**
Ensemble (AdaBoostM1)	**0.71**	**0.79**	**0.72**
Ensemble (LogitBoost)	**0.72**	**0.81**	0.67
Logistic Regression	0.69	0.69	0.69
Naïve Bayes	0.66	0.69	0.69
Neural Network	0.67	0.53	0.55
SVM (Gaussian)	0.69	0.69	0.66
SVM (Linear)	**0.72**	0.69	0.66
SVM (Polynomial)	0.62	0.62	0.59
SVM (Sigmoid)	0.66	0.66	0.45

4. Discussion

We have studied the effects of non-invasive vagus nerve stimulation on the morphology and variability of ECG recordings obtained from participants receiving active taVNS versus sham in tandem with nauseogenic visual stimulation. Our results show, for the first time, that taVNS induces differential effects on ECG-derived SPAR measures when compared to sham. More specifically, we observed marked taVNS-induced reductions in the peak theta density and maximal density both during and following taVNS versus sham stimulation. Our findings further revealed that peak theta density responses after taVNS are linked with reductions in SSQ nausea scores in comparison to sham; and that susceptibility to motion sickness as determined by adult-based motion sickness subjective scores (i.e., MSB scores) was correlated with a taVNS-induced reduction in maximal density responses. Using machine learning with cross-validation, we demonstrated that taVNS response could be detected with above chance level classification performance

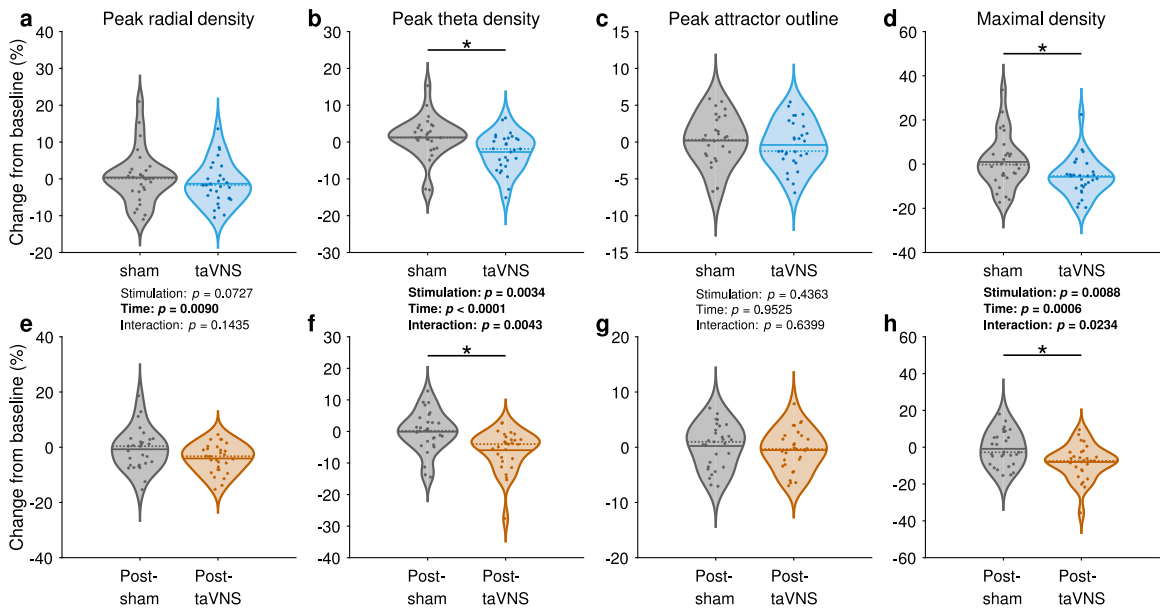

Fig. 5. Attractor features show marked reductions by taVNS versus sham stimulation. (**a–d**) Violin plots showing attractor measures (averaged across all the different embeddings, i.e., $N = 3, 4, 5, 6$) as percentage change from baseline across all participants during sham and taVNS administration. (**e–h**) And following sham and taVNS administration. Each data point represents a participant's attractor measure averaged across the different embeddings. Percentage changes in attractor measures were analyzed with two-way repeated measures ANOVAs with within-subjects factors "time" (pre vs. during vs. post) and "stimulation" (taVNS vs. sham) followed by post-hoc paired *t*-tests using Bonferroni to correct for multiple comparisons when significant interactions were seen. Solid lines indicate mean; dashed lines indicate median.

as measured using the AUC, suggesting a potential avenue for machine models to aid determine whether taVNS has been delivered.

taVNS (20 Hz) administration has been demonstrated previously to prolong sinus cycle length in atrial fibrillation (Stavrakis et al., 2015); most importantly, suggesting that transcutaneous electrical stimulation of the auricular branch of the vagus nerve at the tragus leads to alterations in ECG morphology (shape) and variability. Herein, by using SPAR, we were able to show that taVNS differential effects on ECG shape may be indexed by ECG-derived attractor measures (Fig. 5); in turn, providing initial insights for the hypothesis that this analytical tool may play an important role in facilitating evaluation of taVNS-induced effects on ANS function.

Among all the attractor measures examined, we found that peak theta density appeared to be the most sensitive measure of taVNS response, showing large effect sizes (robust Cohen's $d > 0.8$) in taVNS-induced reductions in attractor density both during and following stimulation. Furthermore, we observed a marked relationship between the peak theta density metric and a significant reduction in motion sickness severity symptoms (as measured by SSQ nausea scores; Table 2), suggesting that reduced attractor density may be a reliable physiological readout of taVNS for motion-induced nausea management. Previous work considered higher attractor densities to convey dynamics in ECG *T* wave morphology (Lyle et al., 2017); hence, we surmise here that taVNS may be inducing shifts in ECG *T* wave morphology and, in turn, ventricular repolarization, thus providing a mechanism by which participants experience less severe malaise with taVNS in contrast to sham.

Our data additionally indicate that taVNS consistently reduced maximal density of the attractors both during and following stimulation (Fig. 5d, h). Importantly, this finding is consistent with evidence showing significantly lower attractor maximal density during vasodilation (Thanaj et al., 2019). Moreover, prior work demonstrated that undergoing a head-up tilt of 60 degrees increases maximal density (Nandi and Aston, 2020); although the sample size was small, the authors suggested that this increase was reflective of reduced waveform variability. From this finding, we can infer that taVNS may be promoting increased ECG variability suggesting potential physiologic utility in taVNS for motion-induced nausea. Indeed, we observed a significant positive correlation between a taVNS-mediated reduction in maximal density and adult-based motion sickness susceptibility scores (that is, MSB scores; Table 2) to suggest that participants with high susceptibility to motion sickness derived the most benefit from taVNS. This has important implications for motion sickness management in individuals well-known to be highly prone to this malady, such as women (Stanney et al., 2020), individuals with history of migraine or vestibular migraine (Wurthmann et al., 2021), including those with history of traumatic brain injury (Classen and Owens, 2010).

While we observed a significant interaction (stimulation × time) between taVNS and sham for the SSQ nausea factor scores, none of the MSAQ responses (MSAQ subscales or total score) revealed marked interactions. It is not clear why this is the case. Previous studies that have used an fMRI-compatible variant of the nauseogenic visual stimulus did not administer the MSAQ alongside the SSQ (e.g., LaCount et al., 2011; Napadow et al., 2013); thus, in the absence of this co-administration of MSAQ and SSQ for the nauseogenic stimulus, our study provides the first data for future studies to compare to. Beyond the nauseogenic stimulus, prior research using a real vehicle (Muth et al., 2006) and head mounted display (Pierre et al., 2015) demonstrated significant differences in both the MSAQ and SSQ, suggesting that with these stimuli, both instruments captured the subjective effects of motion-induced sickness. In this light, a possible explanation for the lack of differences in our study may be that the MSAQ may not extend across stimuli or may not demonstrate consistency in evaluating malaise when nausea induction is performed using the nauseogenic visual stimulus. Another possible explanation can be offered by Czeisler et al. (2023), wherein the authors discussed how the equal weighting of the MSAQ items may influence assessment of motion sickness by increasing the total MSAQ scores in the absence of nausea or vomiting, or decreasing the total MSAQ scores when individuals experience high-malaise symptoms such as severe nausea or vomiting.

Further investigating taVNS response, we show that when trained on a set of ECG-derived attractor features, machine learning models demonstrate differential performance in detecting the electrical stimulation type (taVNS or sham) administered to an individual participant. While the ensemble classifiers outperformed other models when minimizing ten-fold cross-validation loss (Table 3), the LogitBoost classifier

showed higher discriminatory power — achieving an AUC value of 0.81. Importantly, our finding implicates a model trained on attractor features for a role in determining whether stimulation has been delivered properly.

It is also important to remark that although our model's predictive performance is potentially interesting, especially for future taVNS protocols, a model from a tcVNS protocol (Gurel et al., 2020) performed better. This could be attributable to the methodological differences that exist between this previous study and ours; most notably, the notion that taVNS targets the auricular branch of the vagus nerve whereas tcVNS engages the cervical branch. Early evidence showed that tcVNS elicited regional brain activation comparable to that of taVNS (Frangos and Komisaruk, 2017); however, there is currently no study showing that there could be analogous physiological effects on autonomic function between the two modalities. Considering recent evidence for distinct neural pathways revealed by taVNS and invasive cervical VNS from a study using a rodent model (Owens et al., 2024), the implication may be that these modalities influence cardiovascular function differently. On the other hand, a more plausible explanation is the fact that Gurel et al. (2020) performed model training using multimodal inputs of ECG- and PPG-derived variables, which also enabled extraction of a significantly larger feature set (176 features in total) compared to ours (20 features). Indeed, multimodal signal fusion has an important role in machine learning applications for improving model performance (Baltrušaitis et al., 2018); and we acknowledge that our model could have benefited from combining signals from other modalities.

There are several potential limitations to this study. First, although we show feasibility and application of SPAR for evaluating taVNS effects, only a limited number of attractor measures were used; there are numerous features that could be extracted from these attractor images; thus, how those features may respond to taVNS remains unknown. Second, because our participant pool is predominantly female, interpretability of these data may be gender skewed; we advise future studies to take this variable into consideration. Third, recent evidence suggests that taVNS influence on ANS function as indexed by HRV is location- and charge-dependent (Machetanz et al., 2021); thus, despite our taVNS protocol demonstrating differential effects, the stimulation parameters and target examined here could potentially be revised to identify optimal taVNS dosage for maximum protective effects against motion-induced nausea. Another limitation in this study is that we did not perform a blindness assessment; therefore, caution should be exercised when interpreting the findings herein. Further, our study did not include a truly out-of-sample test set and our overall sample size was small; thus, additional caution is warranted when attempting to generalize our findings.

In future studies, we plan to leverage SPAR to identify an optimal taVNS protocol; this may require the use of machine learning techniques given the huge parameter space for taVNS. Moreover, we and others have shown potential for using deep learning for attractor image classification (Aston et al., 2019; Molefi and Palaniappan, 2024); therefore, it would be interesting to study deep neural networks trained on attractor image data toward detection of taVNS therapy response, including identification of effects attributable to taVNS.

5. Conclusions

Here, we document for the first time that taVNS induces differential effects on ECG morphology and variability compared to sham. Reduced peak theta density was found to correlate with improvements in motion-induced nausea severity (indexed by SSQ nausea scores). Moreover, our findings demonstrate that ECG SPAR-based features may have an important role in taVNS therapy response detection; with implications for adaptive taVNS.

CRediT authorship contribution statement

Emmanuel Molefi: Writing – review & editing, Writing – original draft, Visualization, Software, Methodology, Investigation, Formal analysis, Data curation. **Ian McLoughlin:** Writing – review & editing, Supervision, Conceptualization. **Ramaswamy Palaniappan:** Writing – review & editing, Supervision, Conceptualization.

Declaration of competing interest

The authors declare that they have no known competing financial interests or personal relationships that could have appeared to influence the work reported in this paper.

Acknowledgments

E.M. was supported by an Engineering and Physical Sciences Research Council (EPSRC), United Kingdom Ph.D. studentship at the University of Kent School of Computing (EP/T518141/1).

Appendix A. Supplementary data

Supplementary material related to this article can be found online at https://doi.org/10.1016/j.autneu.2025.103318.

Data availability

Data will be made available on request.

References

Aston, P.J., Christie, M.I., Huang, Y.H., Nandi, M., 2018. Beyond HRV: attractor reconstruction using the entire cardiovascular waveform data for novel feature extraction. Physiol. Meas. 39 (2), 024001.

Aston, P.J., Lyle, J.V., Bonet-Luz, E., Huang, C.L., Zhang, Y., Jeevaratnam, K., Nandi, M., 2019. Deep learning applied to attractor images derived from ECG signals for detection of genetic mutation. In: 2019 Computing in Cardiology (CinC). IEEE, pp. 1–4.

Badran, B.W., Dowdle, L.T., Mithoefer, O.J., LaBate, N.T., Coatsworth, J., Brown, J.C., DeVries, W.H., Austelle, C.W., McTeague, L.M., George, M.S., 2018a. Neurophysiologic effects of transcutaneous auricular vagus nerve stimulation (taVNS) via electrical stimulation of the tragus: a concurrent taVNS/fMRI study and review. Brain Stimul. 11 (3), 492–500.

Badran, B., Glusman, C., Badran, A., Austelle, C., DeVries, W., Borckhardt, J., George, M., 2017. The physiological and neurobiological effects of transcutaneous auricular vagus nerve stimulation (taVNS). Brain Stimul.: Basic, Transl. Clin. Res. Neuromodulation 10 (2), 378.

Badran, B.W., Mithoefer, O.J., Summer, C.E., LaBate, N.T., Glusman, C.E., Badran, A.W., DeVries, W.H., Summers, P.M., Austelle, C.W., McTeague, L.M., et al., 2018b. Short trains of transcutaneous auricular vagus nerve stimulation (taVNS) have parameter-specific effects on heart rate. Brain Stimul. 11 (4), 699–708.

Baltrušaitis, T., Ahuja, C., Morency, L.-P., 2018. Multimodal machine learning: A survey and taxonomy. IEEE Trans. Pattern Anal. Mach. Intell. 41 (2), 423–443.

Beh, S.C., Friedman, D.I., 2019. Acute vestibular migraine treatment with noninvasive vagus nerve stimulation. Neurol. 93 (18), e1715–e1719.

Ben-Menachem, E., Manon-Espaillat, R., Ristanovic, R., Wilder, B., Stefan, H., Mirza, W., Tarver, W., Wernicke, J., First International Vagus Nerve Stimulation Study Group, 1994. Vagus nerve stimulation for treatment of partial seizures: 1. A controlled study of effect on seizures. Epilepsia 35 (3), 616–626.

Ben-Menachem, E., Revesz, D., Simon, B., Silberstein, S., 2015. Surgically implanted and non-invasive vagus nerve stimulation: a review of efficacy, safety and tolerability. Eur. J. Neurol. 22 (9), 1260–1268.

Bermejo, P., López, M., Larraya, I., Chamorro, J., Cobo, J., Ordóñez, S., Vega, J., et al., 2017. Innervation of the human cavum conchae and auditory canal: anatomical basis for transcutaneous auricular nerve stimulation. BioMed. Res. Int. 2017.

Bos, J.E., Bles, W., 2004. Motion sickness induced by optokinetic drums. Aviat. Space, Environ. Med. 75 (2), 172–174.

Brainard, D.H., 1997. The psychophysics toolbox. Spat. Vis. 10 4, 433–436.

Butt, M.F., Albusoda, A., Farmer, A.D., Aziz, Q., 2020. The anatomical basis for transcutaneous auricular vagus nerve stimulation. J. Anat. 236 (4), 588–611.

Cao, J., Zhang, Y., Li, H., Yan, Z., Liu, X., Hou, X., Chen, W., Hodges, S., Kong, J., Liu, B., 2021. Different modulation effects of 1 Hz and 20 Hz transcutaneous auricular vagus nerve stimulation on the functional connectivity of the periaqueductal gray in patients with migraine. J. Transl. Med. 19, 1–11.

Carandina, A., Rodrigues, G.D., Di Francesco, P., Filtz, A., Bellocchi, C., Furlan, L., Carugo, S., Montano, N., Tobaldini, E., 2021. Effects of transcutaneous auricular vagus nerve stimulation on cardiovascular autonomic control in health and disease. Auton. Neurosci. 236, 102893.

Classen, S., Owens, A., 2010. Simulator sickness among returning combat veterans with mild traumatic brain injury and/or post-traumatic stress disorder. Adv. Transp. Stud..

Cohen, J., 2013. Statistical Power Analysis for the Behavioral Sciences. Routledge.

Czeisler, M.É., Pruski, J.M., Wang, P., Wang, J., Xiao, C., Polymeropoulos, M.H., Polymeropoulos, V.M., 2023. Validation of the motion sickness severity scale: Secondary analysis of a randomized, double-blind, placebo-controlled study of a treatment for motion sickness. Plos One 18 (1), e0280058.

Dennison, M.S., Wisti, A.Z., D'Zmura, M., 2016. Use of physiological signals to predict cybersickness. Displays 44, 42–52.

Doi, Y., Yoshida, T., Hiroki, T., Arakawa, K., 1983. Effect of mental stress on R wave amplitude of the electrocardiogram in young healthy male subjects. Jpn. Heart J. 24 (2), 189–198.

Ellrich, J., 2019. Transcutaneous auricular vagus nerve stimulation. J. Clin. Neurophysiol. 36 (6), 437–442.

Frangos, E., Komisaruk, B.R., 2017. Access to vagal projections via cutaneous electrical stimulation of the neck: fMRI evidence in healthy humans. Brain Stimul. 10 (1), 19–27.

Gianaros, P.J., Muth, E.R., Mordkoff, J.T., Levine, M.E., Stern, R.M., 2001. A questionnaire for the assessment of the multiple dimensions of motion sickness. Aviat. Space, Environ. Med. 72 (2), 115.

Golding, J.F., 2006. Predicting individual differences in motion sickness susceptibility by questionnaire. Pers. Individ. Differ. 41 (2), 237–248.

Gray, M.A., Taggart, P., Sutton, P.M., Groves, D., Holdright, D.R., Bradbury, D., Brull, D., Critchley, H.D., 2007. A cortical potential reflecting cardiac function. Proc. Natl. Acad. Sci. 104 (16), 6818–6823.

Gresty, M.A., Golding, J.F., 2009. Impact of vertigo and spatial disorientation on concurrent cognitive tasks. Ann. New York Acad. Sci. 1164 (1), 263–267.

Gresty, M.A., Golding, J.F., Le, H., Nightingale, K., 2008. Cognitive impairment by spatial disorientation. Aviat. Space, Environ. Med. 79 (2), 105–111.

Gurel, N.Z., Wittbrodt, M.T., Jung, H., Ladd, S.L., Shah, A.J., Vaccarino, V., Bremner, J.D., Inan, O.T., 2020. Automatic detection of target engagement in transcutaneous cervical vagal nerve stimulation for traumatic stress triggers. IEEE J. Biomed. Heal. Informatics 24 (7), 1917–1925.

Handforth, A., DeGiorgio, C., Schachter, S., Uthman, B., Naritoku, D., Tecoma, E., Henry, T., Collins, S., Vaughn, B., Gilmartin, R., et al., 1998. Vagus nerve stimulation therapy for partial-onset seizures: a randomized active-control trial. Neurology 51 (1), 48–55.

Hilz, M.J., 2022. Transcutaneous vagus nerve stimulation-a brief introduction and overview. Auton. Neurosci. 243, 103038.

Hörandtner, C., Bachler, M., Sehnert, W., Mikisek, I., Mengden, T., Wassertheurer, S., Mayer, C.C., 2022. Attractor reconstruction for quantifying the arterial pulse wave morphology during device-guided slow breathing. Cardiovasc. Eng. Technol. 13 (6), 939–949.

Irmak, T., Pool, D.M., Happee, R., 2021. Objective and subjective responses to motion sickness: the group and the individual. Exp. Brain Res. 239 (2), 515–531.

Kennedy, R.S., Lane, N.E., Berbaum, K.S., Lilienthal, M.G., 1993. Simulator sickness questionnaire: An enhanced method for quantifying simulator sickness. Int. J. Aviat. Psychol. 3 (3), 203–220.

Kim, A.Y., Marduy, A., de Melo, P.S., Gianlorenco, A.C., Kim, C.K., Choi, H., Song, J.-J., Fregni, F., 2022. Safety of transcutaneous auricular vagus nerve stimulation (taVNS): A systematic review and meta-analysis. Sci. Rep. 12 (1), 22055.

Kim, J., Napadow, V., Kuo, B., Barbieri, R., 2011. A combined HRV-fMRI approach to assess cortical control of cardiovagal modulation by motion sickness. In: 2011 Annual International Conference of the IEEE Engineering in Medicine and Biology Society. IEEE, pp. 2825–2828.

Kleiner, M., Brainard, D.H., Pelli, D., 2007. What's new in Psychtoolbox-3? Percept. 36, 1–16.

Lackner, J.R., 2014. Motion sickness: more than nausea and vomiting. Exp. Brain Res. 232, 2493–2510.

LaCount, L.T., Barbieri, R., Park, K., Kim, J., Brown, E.N., Kuo, B., Napadow, V., 2011. Static and dynamic autonomic response with increasing nausea perception. Aviat. Space, Environ. Med. 82 (4), 424–433.

Levine, M.E., Stern, R.M., Koch, K.L., 2014. Enhanced perceptions of control and predictability reduce motion-induced nausea and gastric dysrhythmia. Exp. Brain Res. 232 (8), 2675–2684.

Lyle, J., Aston, P., 2021. Symmetric projection attractor reconstruction: Embedding in higher dimensions. Chaos 31 (11).

Lyle, J.V., Charlton, P.H., Bonet-Luz, E., Chaffey, G., Christie, M., Nandi, M., Aston, P.J., 2017. Beyond HRV: Analysis of ECG signals using attractor reconstruction. In: 2017 Computing in Cardiology (CinC). IEEE, pp. 1–4.

Lyle, J.V., Nandi, M., Aston, P.J., 2019. Investigating the response to dofetilide with Symmetric Projection Attractor Reconstruction of the electrocardiogram. In: 2019 Computing in Cardiology (CinC). IEEE, pp. Page–1.

Lyle, J.V., Nandi, M., Aston, P.J., 2021. Symmetric projection attractor reconstruction: sex differences in the ECG. Front. Cardiovasc. Med. 8, 709457.

Machetanz, K., Berelidze, L., Guggenberger, R., Gharabaghi, A., 2021. Transcutaneous auricular vagus nerve stimulation and heart rate variability: Analysis of parameters and targets. Auton. Neurosci. 236, 102894.

Marcus, D.A., Furman, J.M., Balaban, C.D., 2005. Motion sickness in migraine sufferers. Expert. Opin. Pharmacother. 6 (15), 2691–2697.

Matsangas, P., McCauley, M.E., Becker, W., 2014. The effect of mild motion sickness and sopite syndrome on multitasking cognitive performance. Hum. Factors 56 (6), 1124–1135.

Molefi, E., McLoughlin, I., Palaniappan, R., 2023a. Heart Rate Variability Responses to Visually Induced Motion Sickness. In: 2023 45th Annual International Conference of the IEEE Engineering in Medicine & Biology Society. EMBC, IEEE, pp. 1–4.

Molefi, E., McLoughlin, I., Palaniappan, R., 2023b. On the potential of transauricular electrical stimulation to reduce visually induced motion sickness. Sci. Rep. 13 (1), 3272.

Molefi, E., Palaniappan, R., 2024. Deep Transfer Learning for Visually Induced Motion Sickness Detection Using Symmetric Projection Attractor Reconstruction of the Electrocardiogram. In: 2024 Computing in Cardiology (CinC). 51, IEEE, pp. 1–4.

Murray, A.R., Atkinson, L., Mahadi, M.K., Deuchars, S.A., Deuchars, J., 2016. The strange case of the ear and the heart: the auricular vagus nerve and its influence on cardiac control. Auton. Neurosci. 199, 48–53.

Muth, E.R., Walker, A.D., Fiorello, M., 2006. Effects of uncoupled motion on performance. Hum. Factors 48 (3), 600–607.

Nandi, M., Aston, P.J., 2020. Extracting new information from old waveforms: Symmetric projection attractor reconstruction: Where maths meets medicine. Exp. Physiol. 105 (9), 1444–1451.

Nandi, M., Venton, J., Aston, P.J., 2018. A novel method to quantify arterial pulse waveform morphology: attractor reconstruction for physiologists and clinicians. Physiol. Meas. 39 (10), 104008.

Napadow, V., Sheehan, J.D., Kim, J., LaCount, L.T., Park, K., Kaptchuk, T.J., Rosen, B.R., Kuo, B., 2013. The brain circuitry underlying the temporal evolution of nausea in humans. Cerebral Cortex 23 (4), 806–813.

Owens, M.M., Jacquemet, V., Napadow, V., Lewis, N., Beaumont, E., 2024. Brainstem neuronal responses to transcutaneous auricular and cervical vagus nerve stimulation in rats. J. Physiol..

Pan, J., Tompkins, W.J., 1985. A Real-Time QRS Detection Algorithm. IEEE Trans. Biomed. Eng. BME-32 (3), 230–236.

Pelli, D., 1997. The VideoToolbox software for visual psychophysics: transforming numbers into movies. Spat. Vis. 10 4, 437–442.

Peuker, E.T., Filler, T.J., 2002. The nerve supply of the human auricle. Clin. Anat. 15 (1), 35–37.

Pierre, M.E.S., Banerjee, S., Hoover, A.W., Muth, E.R., 2015. The effects of 0.2 Hz varying latency with 20–100 ms varying amplitude on simulator sickness in a helmet mounted display. Displays 36, 1–8.

Sclocco, R., Kim, J., Garcia, R.G., Sheehan, J.D., Beissner, F., Bianchi, A.M., Cerutti, S., Kuo, B., Barbieri, R., Napadow, V., 2016. Brain circuitry supporting multi-organ autonomic outflow in response to nausea. Cereb. Cortex 26 (2), 485–497.

Stanney, K., Fidopiastis, C., Foster, L., 2020. Virtual reality is sexist: but it does not have to be. Front. Robot. AI 7, 4.

Stavrakis, S., Humphrey, M.B., Scherlag, B.J., Hu, Y., Jackman, W.M., Nakagawa, H., Lockwood, D., Lazzara, R., Po, S.S., 2015. Low-level transcutaneous electrical vagus nerve stimulation suppresses atrial fibrillation. J. Am. Coll. Cardiol. 65 (9), 867–875.

Takens, F., 1981. Detecting strange attractors in turbulence. In: Dynamical Systems and Turbulence, Warwick 1980. In: Lecture Notes in Mathematics, vol. 898, pp. 366–381.

Thanaj, M., Chipperfield, A.J., Clough, G.F., 2019. Attractor reconstruction analysis for blood flow signals. In: 2019 41st Annual International Conference of the IEEE Engineering in Medicine and Biology Society. EMBC, IEEE, pp. 2281–2284.

Toschi, N., Kim, J., Sclocco, R., Duggento, A., Barbieri, R., Kuo, B., Napadow, V., 2017. Motion sickness increases functional connectivity between visual motion and nausea-associated brain regions. Auton. Neurosci. 202, 108–113.

Tran, N., Asad, Z., Elkholey, K., Scherlag, B.J., Po, S.S., Stavrakis, S., 2019. Autonomic neuromodulation acutely ameliorates left ventricular strain in humans. J. Cardiovasc. Transl. Res. 12, 221–230.

Wurthmann, S., Naegel, S., Roesner, M., Nsaka, M., Scheffler, A., Kleinschnitz, C., Holle, D., Obermann, M., 2021. Sensitized rotatory motion perception and increased susceptibility to motion sickness in vestibular migraine: A cross-sectional study. Eur. J. Neurol. 28 (7), 2357–2366.

Yakunina, N., Kim, S.S., Nam, E.-C., 2017. Optimization of transcutaneous vagus nerve stimulation using functional MRI. Neuromodulation: Technol. Neural Interface 20 (3), 290–300.